Solid Freeform Fabrication 2021: Proceedings of the 32nd Annual International Solid Freeform Fabrication Symposium – An Additive Manufacturing Conference
Reviewed Paper

In-Situ Thermographic Inspection for Laser Powder Bed Fusion

T. Liu[1], C.S. Lough[1], H. Sehhat[1], J. Huang[2], E.C. Kinzel[3], M.C. Leu[1]

[1]Mechanical and Aerospace Engineering Department, Missouri University of Science and Technology, Rolla, MO 65409, USA

[2]Electrical and Computer Engineering Department, Missouri University of Science and Technology, Rolla, MO 65409, USA

[3]Aerospace and Mechanical Engineering Department, University of Notre Dame, Notre Dame, IN 46556, USA

Abstract

Laser powder bed fusion is strongly influenced by the quality of the powder layer including the powder properties as well as the layer thickness. In particular, thermal stresses can produce sufficient part deformation to the point that a part interferes with the wiper. This paper investigates the use of long-wave infrared thermography to monitor the surface temperature of the build. When cold powder is spread by the wiper, heat diffuses from the underlying part through the powder. The surface temperature history is a strong function of the thermal transport properties of the powder as well as the thickness. This correlation is explored and measured experimentally. It is then used to estimate the powder layer thickness above overhanging parts. This approach is shown to capture the part distortion and predicts wiper state prior to catastrophic interaction with the part.

Keywords: Laser powder bed fusion, long wavelength infrared, powder thickness

1. Introduction

Laser powder bed fusion (LPBF), as one of the most common additive manufacturing technologies, is a process that melts a metal powder by a high-power laser beam layer by layer to generate 3D metal parts [1-3]. The powder layer properties affect the product performance significantly. For example, the microhardness decreases, and the grain size increases for 1Cr18Ni9Ti stainless steel powder when the layer thickness increases in the range of 60 – 100 μm [4]. However, for the CL50WS powder, powder layer thickness in the range of 30 - 40 μm has no significant influence on microhardness [5-6]. Other mechanical properties of the fabricated parts may also be sensitive to powder properties. For the parts produced from Ti-6Al-4V powder, rapid increase in porosity and surface roughness may result from the use of thick powder layer above 40 μm [7].

In-situ measurement of powder layer thickness has attracted many researchers' attention in recent years. Richard et al. developed a laser displacement in-situ non-destructive method to measure the top powder layer thickness [8]. There are other optical in-situ methods to measure the top powder surface profile. For example, the high-speed spectral domain optical coherence tomography (SD-OCT) was used to measure the layer roughness [9]. The digital fringe projection technique was implemented to measure the surface topography of powder layer [10]. Although these optical approaches can measure the powder layer thickness, none of them can provide the powder thermal conductivity information based on their in-situ measurement data.

Thermal cameras and imaging approaches have been used to monitor thermal features during LPBF manufacturing [11]. Short-wavelength infrared (SWIR) cameras, which are more sensitive at high temperature, have been used to monitor the melt-pool dynamics and stability [12], cooling rate [13], and combined with visible cameras to monitor defects [14]. In contrast, relatively inexpensive, uncooled long-wavelength infrared (LWIR) cameras, which are more sensitive at lower temperature, have been used to observe the plume formed by material evaporation and heating of the surrounding gas [15], obtain the surface temperature and cooling time [16], and predict the temperature distribution [17]. Furthermore, image data has been combined with machine learning algorithms to provide an efficient means to assess part quality, validate specific internal geometries, and detect build defects [18,19]. However, no previous researchers have used LWIR cameras to measure in-situ the powder layer thickness and thermal conductivity. The study described in the present paper fills this significant gap.

In this study, a LWIR camera is used to monitor the temperature of the powder bed during the LPBF process. By analyzing the thermography data, the temperature profile is calculated from the thermal history, and the temperature rise time is mapped to the powder layer thickness based on 1D thermal modeling. The obtained powder

layer thickness has been verified experimentally. Finally, an application of the in-situ thermographic monitoring for recoater jam prediction is demonstrated.

2. Experimental setup

Renishaw AM250, which is an additive manufacturing machine that fabricates metal parts by using the LPBF process, was used to manufacture 304L stainless steel samples. An FLIR A655sc LWIR camera was installed in a Renishaw AM250 machine at the Missouri University of Science and Technology. Figure 1a shows the experimental setup. The ZnSe window locates in front of the LWIR camera was used to seal the build chamber. Figure 1b shows an example of the camera field of view.

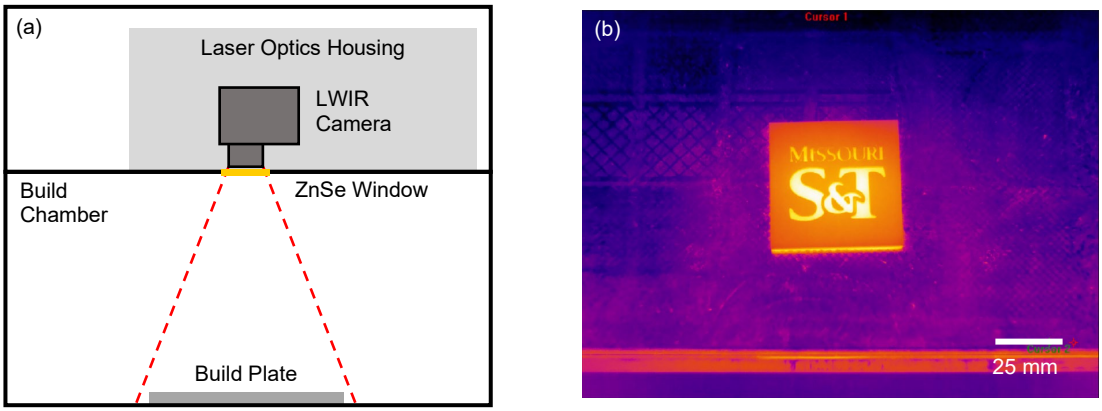

Fig. 1. (a) LWIR image of blackbody during cooling and (b) reference visible image of experimental setup.

Since the 304L stainless steel powder bed and LPBF printed solid part have different emissivity, the radiance recorded by the infrared camera needs to be calibrated for both the powder bed and the solid part. Our calibration experiment is shown in Fig. 2. A LPBF 304L stainless steel bin with a cavity in it is manufactured to the equivalent of a blackbody. 304L powder was placed partially on the bin's top surface, and the bin surface remained observable from the infrared camera. This blackbody was heated by the AM250 laser with 200W for seconds at a time as shown in Fig. 2a schematic. This design configuration permitted the simultaneous temperature calibration for the blackbody, 304L stainless steel powder, and 304L solid bin. The LWIR image shown in Fig. 2a denotes the temperature distribution during cooling, and a visible image of the experimental setup is shown in Fig. 2b. The $T_{apparent}$ is the temperature measured by the thermal camera single pixel. The actual temperature T_{actual} of the blackbody was recorded by thermocouples located at the top and bottom of the calibration cube. The average of the two thermocouple values is plotted as the actual temperature in the heating and cooling curve shown in Fig. 3(a). The corresponding $T_{apparent}$ temperatures for the various material states were measured with the LWIR camera. These results are included in Fig. 3(b).

In the cooling process, the various material states have the same temperature. However, the different emissivity of these various states make the apparent temperatures recorded by the camera different as shown in Fig. 3(b). The cooling portions of the curves in Fig. 3(b) were used to develop the calibrations from the apparent temperature to the actual temperature. These results are included as Fig. 4 and show that the actual temperature scales linearly with the apparent temperature for all the blackbody, the 304L powder, and the 304L solid. The different calibration equations obtained are:

$$\begin{aligned} T_{blackbody} &= T \times 5.83 - 101.67 \\ T_{solid} &= T \times 14.84 - 310.28 \\ T_{powder} &= T \times 7.64 - 144.38 \end{aligned} \tag{1}$$

These calibration equations will be used to determine the actual temperatures from the measured apparent temperature.

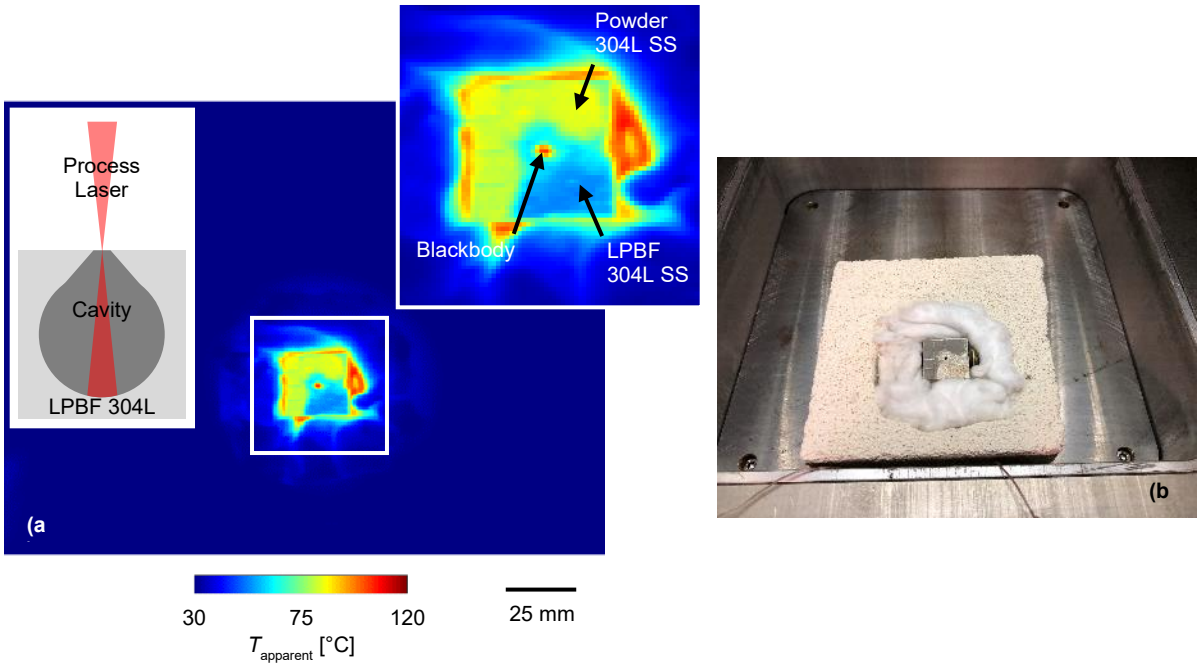

Fig. 2. (a) LWIR image of blackbody during cooling and (b) reference visible image of experimental setup.

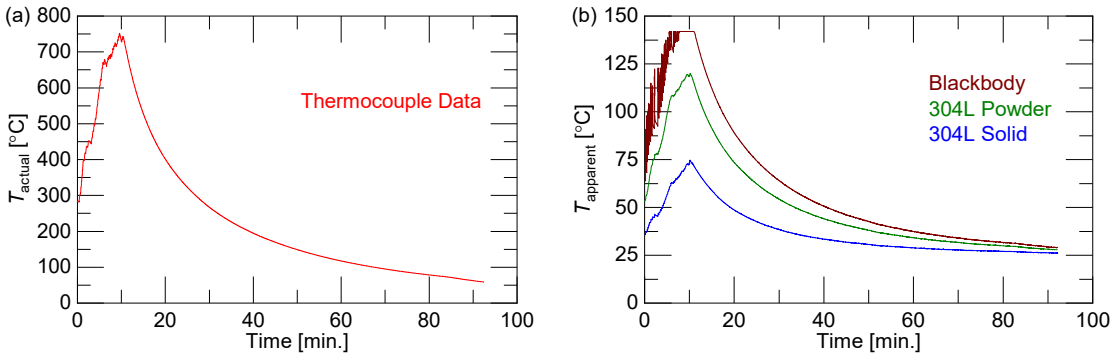

Fig. 3. Blackbody heating and cooling curves with (a) actual temperature from thermocouple measurements and (b) apparent temperature from various locations in LWIR data.

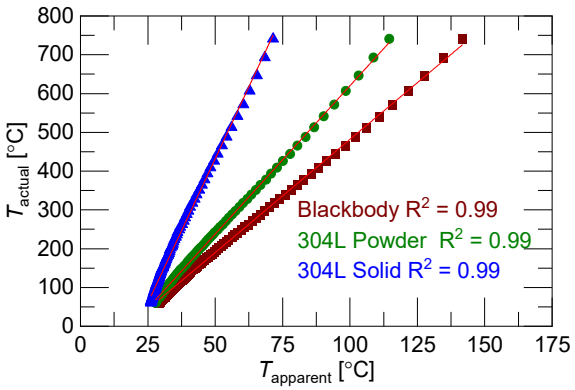

Fig. 4. LWIR temperature calibrations for blackbody material, 304L stainless steel powder, and 304L stainless steel solid.

3. LWIR camera data processing

3.1 Thermal history

The specimens of 304L stainless steel were manufactured by the Renishaw AM250 and recorded by layer-to-layer LWIR imaging. The laser in Renishaw AM250 scans the powder parts with a point-to-point exposure strategy. This scanning process steps discretely with the parameters of point distance, exposure time, and hatch spacing. The laser scanning has a fixed orientation perpendicular to wiper moving direction and there was no rotation of the scanning direction from layer to layer. The wiper is located in front of the build plane during the laser scanning fabrication. After the laser finishes the scanning of one layer, the wiper returns to the powder delivery hopper at the back side of the build plane. Then the wiper obtains the fresh powder from the powder delivery hopper, and it goes forward to spread a fresh layer of powder. This process is shown in Fig. 5. The experiment parameter sets are laser power 200W, exposure time 50 μs, point distance 60 μm, hatch spacing 85 μm, and powder thickness 50 μm. The build plate is heated to 80°C during the LPBF process. The entire build chamber is filled with Argon gas to avoid oxidation.

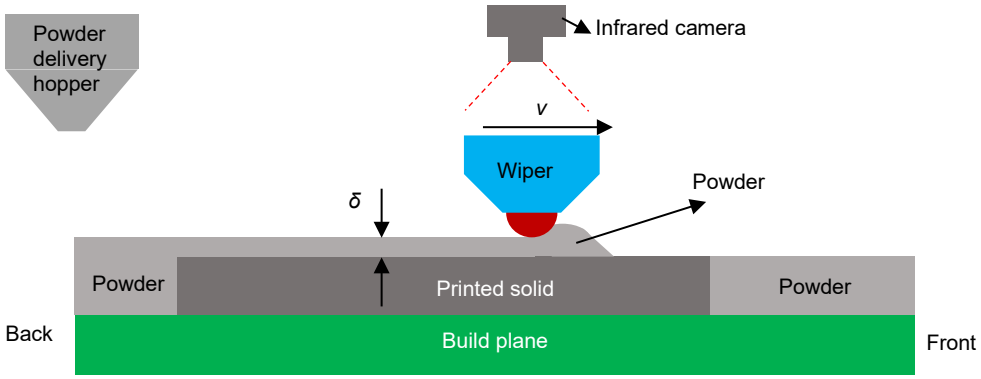

Fig. 5. Schematic of powder spreading process

The thermal histories of laser printing with the calibration equations in Eq. (1) are shown in Fig. 6a. When the build plate's top surface is covered by powder, the thermal history needs to be calibrated using the powder emissivity. Similarly, when the powder is melt and then solidified, the solid emissivity should be used. Fig. 6b shows this calibration results. In Fig. 6a, the left-valley minimum temperature indicates the wiper temperature when the wiper is spreading the powder. When the wiper obtains the fresh powder from the powder delivery hopper, it moves to the front to spread a fresh layer of powder with 50 μm height. The newly spread powder is heated by the printed layer underneath. The temperature rise curve after the left valley represents this temperature heat-up process. After this spread, the wiper stays at the front of build plate during the laser printing. The temperature at the peak represents the laser heating the powder bed and melting the powder. After the laser printing, the wiper goes back to the powder delivery hopper. The right-valley minimum temperature in the thermal history indicates the wiper temperature when the powder is covered by the wiper during its traveling back. There is a slight temperature rise when wiper return. This is because when wiper return, it respread tiny powder on the top of printed solid area.

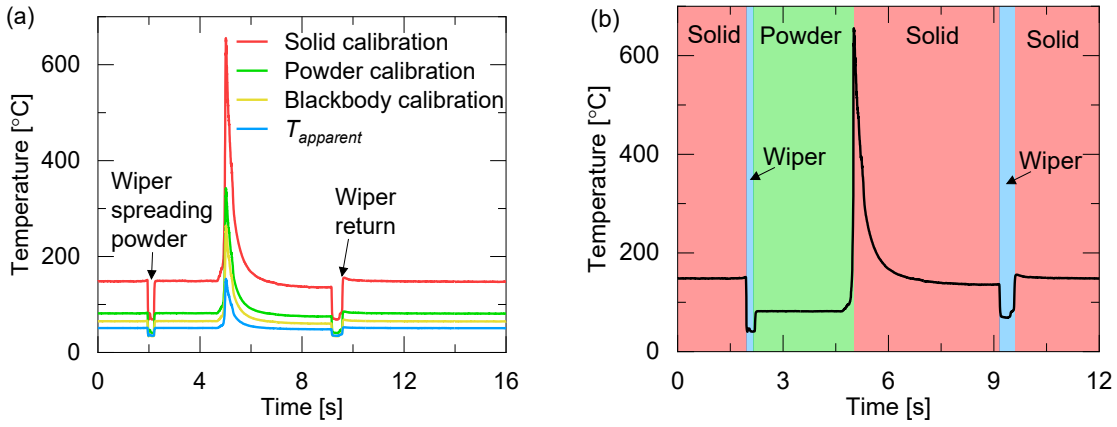

Fig. 6. (a) Temperature history obtained by using different calibration equations, (b) calibrated temperature history.

The powder temperature heat-up process is valuable because it relates to the powder properties: the temperature of a thinner powder layer rises faster than the temperature of a thicker powder layer.

3.2 1D heat transfer model

In order to understand the effect of powder properties, a one-dimensional heat transfer model is established. A schematic of the 1D heat transfer model is shown in Fig. 7a. There are two finite slabs with thickness δ and s representing the powder and printed solid parts. The powder slab is assumed in perfect contact with the printed solid slab. The x-coordinates x_p and x_s for the powder and solid slabs are conveniently chosen as shown in the figure. The equation describing unsteady 1D heat conduction and the initial and boundary conditions for the powder slab in x_p-coordinate are given by

$$\frac{\partial T_1}{\partial t} = \frac{k_p}{C_p \rho_p} \frac{\partial^2 T_1}{\partial x_p^2} \tag{2}$$

$$T_1(\delta, t) = T_i(t) \tag{3}$$

$$k_p \left. \frac{\partial T_1}{\partial x_p} \right|_{x=0} = h\left[T_1(0,t) - T_\infty\right] \tag{4}$$

$$T_1\left(x_p, 0\right) = T_p \tag{5}$$

where T_1 is the temperature distribution of powder, t is time, x_p is the distance normal to the build plane, k_p is the thermal conductivity of powder, C_p is the specific heat capacity of powder, ρ_p is the density of powder, δ is the thickness of powder layer, T_i is the interface temperature, T_∞ is the ambient temperature, h is the convective heat transfer coefficient of gas, T_p is the initial temperature of powder. The radiation loss occurred at the powder top surface is assumed negligible.

The finite difference method is used to solve the above equations for the temperature distribution for a given powder thickness. The obtained temperature distributions for several powder thicknesses are shown in Fig. 7b and 7c, where the material properties used are given in Table 1. The T_∞ is 30°C as the temperature of the Argon gas. T_s is 80°C as the build plate heating temperature. T_p is 30°C as same as T_∞, h is 15 W/m^{2}K, s is 3mm.

Table 1 Material properties of 304L solid and powder

Properties	304L Solid	304L Powder
Density ρ [kg/m^3]	8030	4818
Specific heat capacity c [J/kg•K]	490	490
Therma conductivity k [W/m•K]	16.2	0.13

Figure 7b shows the temperature history of the powder top surface for different powder thicknesses. The temperature of a thicker powder layer rises more slowly than the temperature of a thinner powder layer. Fig. 7c shows the temperature distribution along the depth direction. It shows that the powder surface temperature reaches almost T_s in 1s.

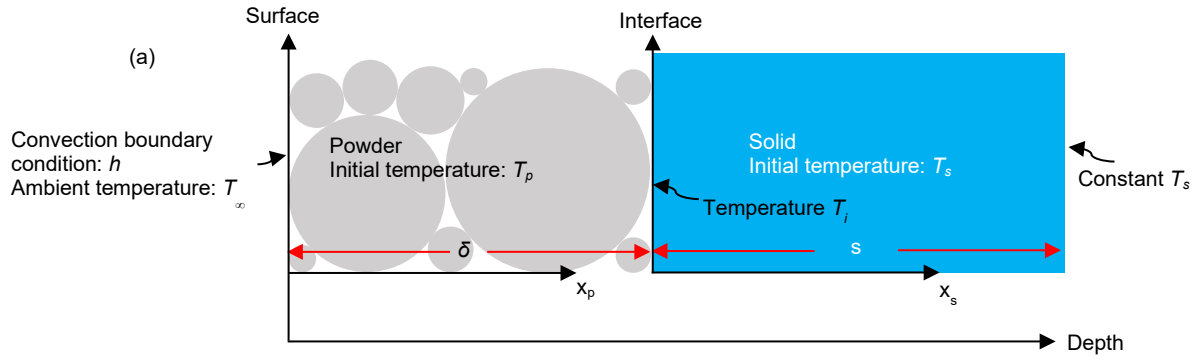

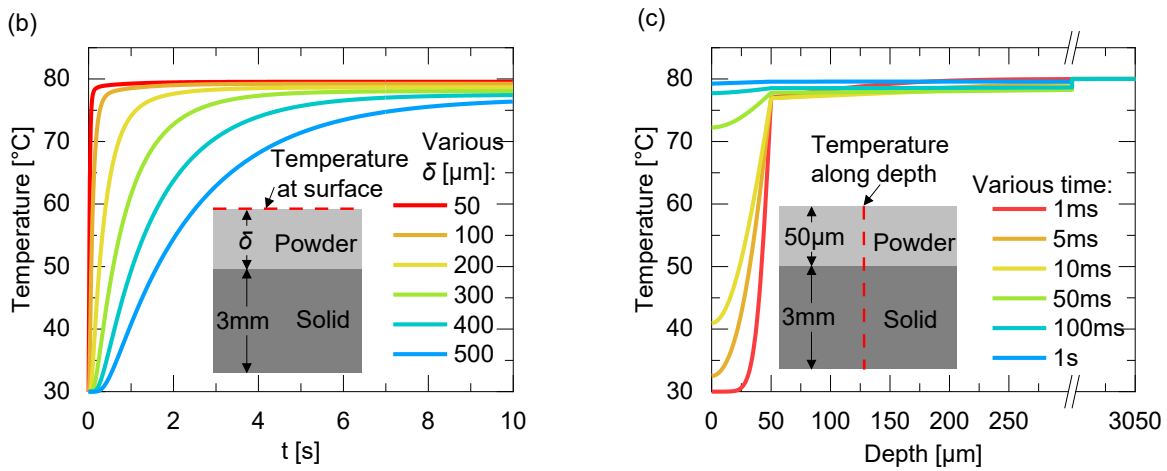

Fig. 7. (a) Schematic image of 1D heat transfer model, (b) top surface thermal history (c) and temperature distribution at various time instants.

4. Correlation of thermal features with powder properties

4.1 Rise time

The heat-up curves in Fig. 7b are examined carefully in order to express them in mathematical equations. It is observed that a liner combination of a constant and two exponential functions with different coefficients can be used to fit the temperature rise very well. The expression of this fitting function is

$$T = \begin{cases} A_1 - A_2 e^{-\alpha_1 t} - A_3 e^{-\alpha_2 t} & t > t_i \\ A_1 - A_2 - A_3 & t < t_i \end{cases} \tag{6}$$

This is a piecewise function. A_1 is the powder's steady-state temperature. A_1-A_2-A_3 is the powder's initial temperature. α_1 can be very large to represent the initial rapid heat-up process and α_2 is smaller to represent the speed of approaching the steady-state temperature. t_i is the time that the powder starts to heat up. By using this function, the temperature rise curves in Fig. 7b can be fitted very well as shown in Fig. 8a. The purpose of constructing this fitting function is to obtain the temperature rise time. The temperature rise time is defined here as the time period from the initial time to the time when temperature reaches 90% of the steady-state temperature. The rise time can be obtained by solving the equation:

$$A_2 e^{-\alpha_1 t} + A_3 e^{-\alpha_2 t} = 0.1\left(A_2 + A_3\right) \tag{7}$$

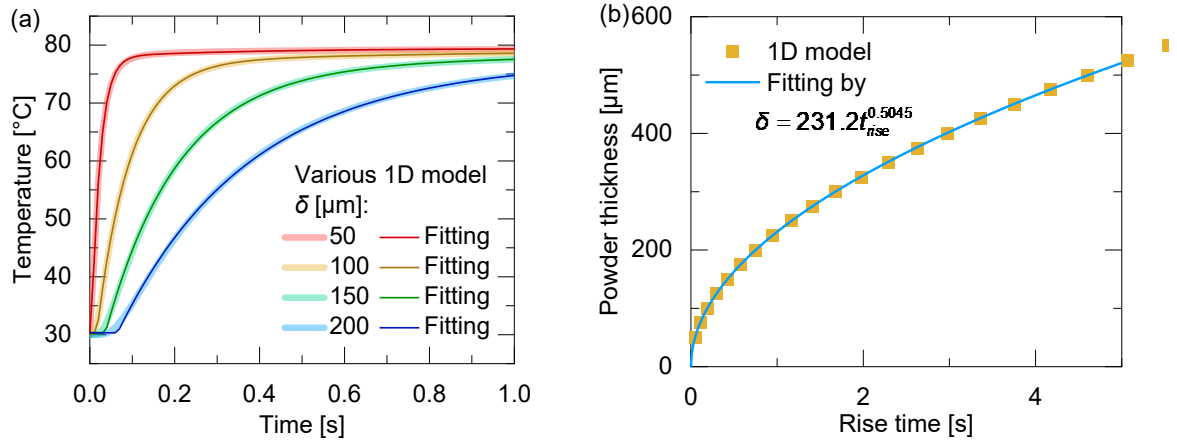

Fig. 8. (a) Comparison between 1D model thermal history with fitting result and (b) powder thickness with respect to rise time calculated from 1D model.

The rise time of different powder thickness calculated by the 1D model is shown in Fig. 8b with respect to the powder thickness. It is clear that the relationship between powder thickness and temperature rise time is monotonic, and it can be represented by the following exponential function:

$$\delta = 231.2 t_{rise}^{0.5045} \tag{8}$$

By using this exponential function, the powder layer thickness can be calculated from its temperature rise time.

4.2 Powder properties

Equation 8 shows the relationship between powder thickness and temperature rise time calculated by using 1D heat transfer model. This relationship needs to be validated experimentally. The specimens with different heights were fabricated by the AM250 machine for the validation experiment. As shown in Fig. 10, there are 4 identical specimens, each having 8 strips with different heights. Fig. 9a shows the profile of 8 different heights and Table 2 lists the strip heights and the corresponding powder thickness for every strip. After this experiment, the build plate was taken out of the build chamber and its precise dimensions was measured by laser scanning. The powder layer thickness above every strip can be calculated as the total powder thickness subtracts the specimen's height. The 2D map of powder layer thickness is shown in Fig. 9c.

Table 2 The height of each of the eight different strips and corresponding powder thickness

n	h [mm]	δ [μm]
1	5.00	50
2	4.75	300
3	4.65	400
4	4.90	150
5	4.70	350
6	4.85	200
7	4.80	250
8	4.95	100

To measure the temperature rise, when the manufacture of these 4 specimens was done and before moved it out, the build plate was kept in the Renishaw AM250 build chamber's original position. Then the 4 specimens' top surfaces were cleaned. After cleaning specimens' surface powder and keeping the build plate temperature at 80°C, a new fresh layer was spread by the wiper to cover all the 4 specimens' top surfaces. Since the fresh powder has a lower temperature T_p and the specimens have different heights, the specimen strips with higher heights have thinner fresh powder to heat up. The fresh powder was heated up at different speeds at various locations. The infrared camera recorded the process of temperature rise for all the height strips. Then Eq. 6 was used to fit all the temperature history and Eq. 7 was used to calculate the rise time. The final 2D map of the rise time is shown in Fig. 10a.

Figure 11a shows the temperature rise curves at four different positions on a specimen's top surface. The fitting curves obtained by Eq. 6 match very well with the temperatures measured by the LWIR camera. The data of mean powder thicknesses vs. temperature rise time for each of the 8 strips in the four specimens from Fig. 9c and 10a are plotted in Fig. 11b. The error bars indicate the standard deviation. The power function obtained to fit these mean values by regression is

$$\delta = 218.6 t_{rise}^{0.58}. \tag{9}$$

Note that the values of coefficients in this function from experiment are close to the values of coefficients obtained previously 1D model for Eq. 8. The difference is caused by the rise time calculation. The 2D map of powder thickness can be calculated from Eq. 9 and is shown in Fig. 10b.

In order to compare the powder thickness predicted by Eq. 9 with measured powder thickness, data of Fig. 9c and Fig. 10b are plotted together as show in Fig. 11. The R^2 for this prediction results is 0.7641.

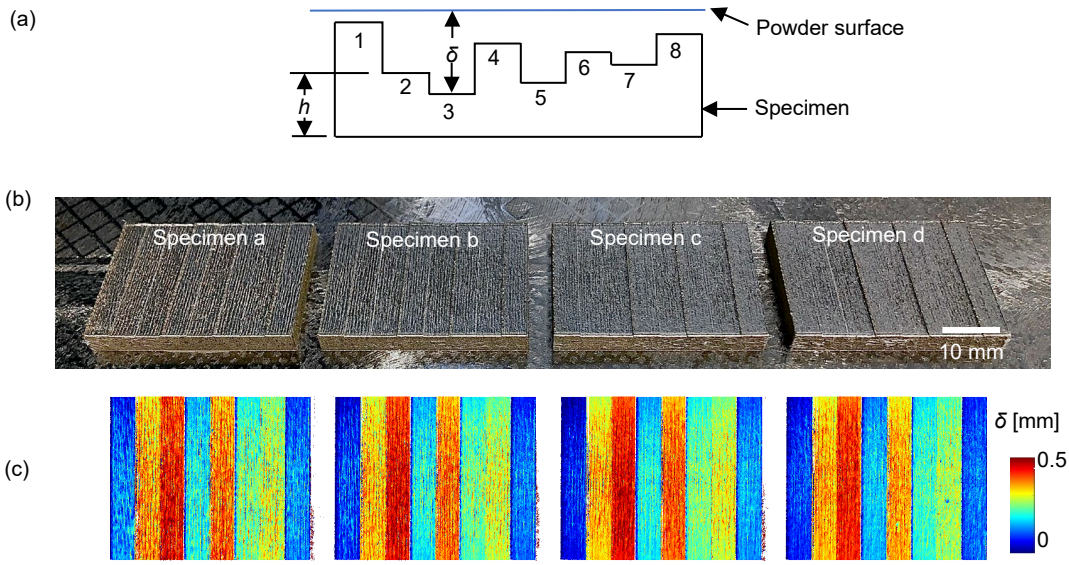

Fig. 9. (a)Surface profile of one specimen with 8 different strips, (b) Images of four specimens, each divided into eight strips with different heights (c) 2D map of the powder thickness.

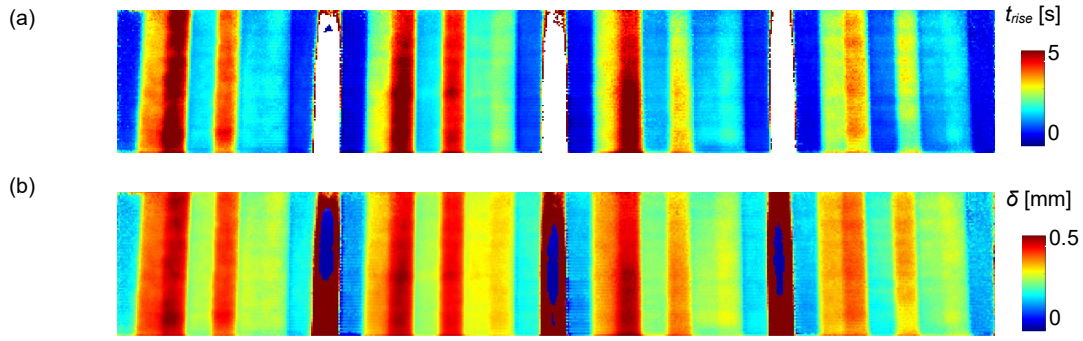

Fig. 10. (a) 2D map of the temperature rise time for different regions of the specimens and (b) 2D map of the powder thickness calculated by Eq. 9.

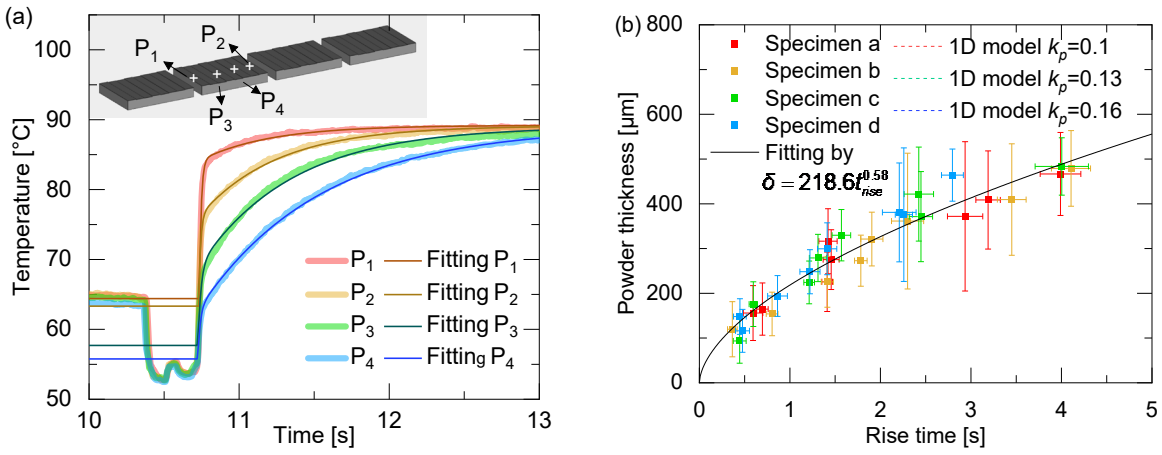

Fig. 11. (a) Comparison between measured temperatures with fitting results and (b) powder thickness with respect to temperature rise time from experimental data.

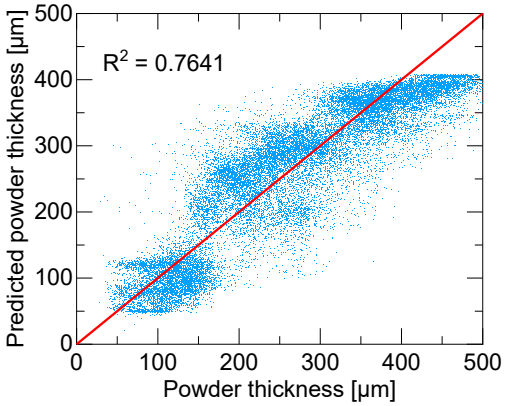

Fig. 12. Comparison between measured powder thickness with respect to powder thickness predicted by rise time

5. Application of the in-situ thermographic monitoring for recoater jam prediction

The thermographic inspection of powder thickness is applied for recoater jam prediction and prevention in the LPBF process. Because of the residual stresses occurred in the parts during LPBF manufacturing, overhanging parts always curl up. The deformation grows faster on the overhanging part's contour than its interior. The part curl-up after deformation over a threshold can hit the wiper and cause serious consequences. Hence, prediction and prevention of the recoater jam in real-time LPBF manufacture is necessary. A recoater jam prediction system has been established based on calculating the powder layer thickness at different locations of the powder bed. When the curl-up deformation grows, the powder layer at the curl-up location becomes thinner and thinner and eventually will damage the wiper and cause the recoater jam. The powder layer thickness can be used to represent the amount of curl-up. To demonstrate this application, overhanging semi-arches are manufactured, and the corresponding powder thicknesses are calculated. The nominal layer thickness is 50 μm. Figure 13a shows the calculated powder thickness at the right edge of each of two semi-arches shown from the first layer to the occurrence of recoater jam. The curve has four different regions. In the initial region shown by the light blue area, the powder thickness increases. In the green region from layer 50 to layer 170, the powder thickness keeps essentially constant. In the yellow region, the powder thickness drops (decreases quickly) from layer 170 to layer 215. In the pink (last) region, the recoater jam occurred and powder thickness fluctuates wildly. Fig. 13b shows the final states of five semi-arches and the ablated wiper in the experiment. The silicone part of the wiper is ablated by the semi-arch deformations, and the metal parts of wiper behind silicone are scratched too.

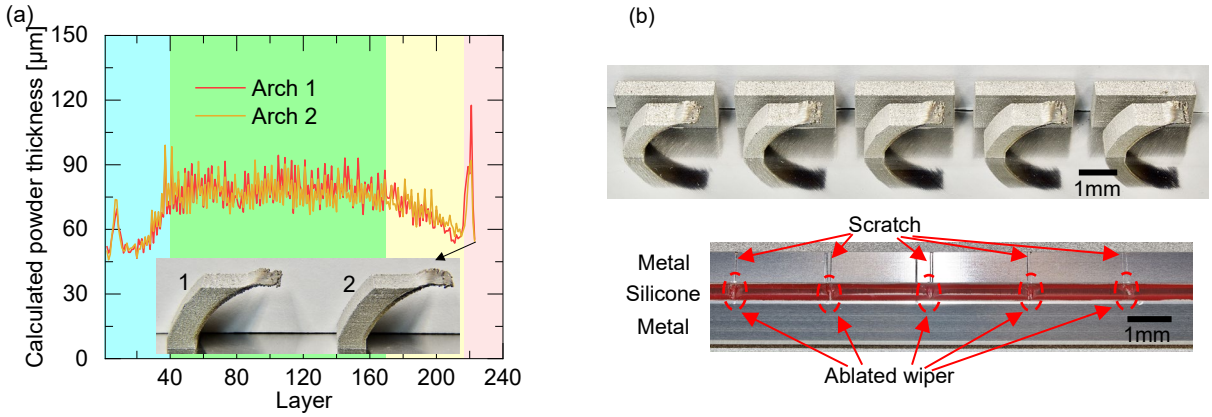

Fig. 13. (a) Real-time calculated powder thickness and (b) final semi-arch samples and the ablated wiper.

6. Conclusion

This paper presents using a LWIR camera to perform in-situ powder layer thickness during metal additive manufacturing processes. A 1D powder layer heat transfer model was developed and solved using the finite difference method, from which the calculation of rise time profile from temperature distribution in the powder was made. The method of mapping temperature rise time to powder layer thickness was illustrated. The 1D model of temperature rise time vs. powder thickness agrees well with validation experimental result. The application of this thermographic inspection method for overhang curl-up detection and recoater jam prevention was demonstrated.

7. Acknowledgements

The authors would like to thank Honeywell for its leading role on this research project and UCLA for the cooperative efforts. The financial support for this research is provided by the Clean Energy Smart Manufacturing Innovation Institute (CESMII).

8. References

1. Lough, Cody S., Xin Wang, Christopher C. Smith, Robert G. Landers, Douglas A. Bristow, James A. Drallmeier, Ben Brown, and Edward C. Kinzel. "Correlation of SWIR imaging with LPBF 304L stainless steel part properties." Additive Manufacturing 35 (2020): 101359.
2. Hung, Chia-Hung, Wei-Ting Chen, M. Hossein Sehhat, and Ming C. Leu. "The effect of laser welding modes on mechanical properties and microstructure of 304L stainless steel parts fabricated by laser-foil-printing additive manufacturing." The International Journal of Advanced Manufacturing Technology 112, no. 3 (2021): 867-877.
3. Mahdianikhotbesara, Ali, M. Hossein Sehhat, and Mohammadjafar Hadad. "Experimental Study on Micro-Friction Stir Welding of Dissimilar Butt Joints Between Al 1050 and Pure Copper." Metallography, Microstructure, and Analysis (2021): 1-16.
4. Ma, Mingming, Zemin Wang, Ming Gao, and Xiaoyan Zeng. "Layer thickness dependence of performance in high-power selective laser melting of 1Cr18Ni9Ti stainless steel." Journal of Materials Processing Technology 215 (2015): 142-150.
5. Yasa, Evren, Karolien Kempen, J. Kruth, Lore Thijs, and Jan Van Humbeeck. "Microstructure and mechanical properties of maraging steel 300 after selective laser melting." In Solid freeform fabrication symposium proceedings, pp. 383-396. 2010.
6. Kempen, Karolien, Evren Yasa, Lore Thijs, J-P. Kruth, and Jan Van Humbeeck. "Microstructure and mechanical properties of Selective Laser Melted 18Ni-300 steel." Physics Procedia 12 (2011): 255-263.
7. Qiu, Chunlei, Chinnapat Panwisawas, Mark Ward, Hector C. Basoalto, Jeffery W. Brooks, and Moataz M. Attallah. "On the role of melt flow into the surface structure and porosity development during selective laser melting." Acta Materialia96 (2015): 72-79.
8. Williams, Richard J., Catrin M. Davies, and Paul A. Hooper. "In situ monitoring of the layer height in laser powder bed fusion." Material Design & Processing Communications.
9. DePond, Philip J., Gabe Guss, Sonny Ly, Nicholas P. Calta, Dave Deane, Saad Khairallah, and Manyalibo J. Matthews. "In situ measurements of layer roughness during laser powder bed fusion additive manufacturing using low coherence scanning interferometry." Materials & Design 154 (2018): 347-359.
10. Zhang, Bin, John Ziegert, Faramarz Farahi, and Angela Davies. "In situ surface topography of laser powder bed fusion using fringe projection." Additive Manufacturing 12 (2016): 100-107.
11. Lane, Brandon, Eric Whitenton, and Shawn Moylan. "Multiple sensor detection of process phenomena in laser powder bed fusion." In Thermosense: Thermal Infrared Applications XXXVIII, vol. 9861, p. 986104. International Society for Optics and Photonics, 2016.
12. Hooper, P. A. Melt pool temperature and cooling rates in laser powder bed fusion. Addit Manuf 22, 548–559 (2018).
13. Heigel, Jarred C., and Eric Whitenton. "Measurement of thermal processing variability in powder bed fusion." In Proceedings of the 2018 ASPE and Euspen Summer Topical Meeting-Advancing Precision in Additive Manufacturing, Berkeley, CA, USA, pp. 22-25. 2018.
14. Colosimo, B. M., Grossi, E., Caltanissetta, F. & Grasso, M. Penelope: A Novel Prototype for In Situ Defect Removal in LPBF. Jom-us 72, 1332–1339 (2020).
15. Grasso, M. & Colosimo, B. M. A statistical learning method for image-based monitoring of the plume signature in laser powder bed fusion. Robot Cim-int Manuf 57, 103–115 (2019).

16. Yavari, M. R., Williams, R. J., Cole, K. D., Hooper, P. A. & Rao, P. Thermal Modeling in Metal Additive Manufacturing Using Graph Theory: Experimental Validation With Laser Powder Bed Fusion Using In Situ Infrared Thermography Data. J Manuf Sci Eng 142, (2020).
17. Yavari, Reza, Richard Williams, Alex Riensche, Paul A. Hooper, Kevin D. Cole, Lars Jacquemetton, Harold Scott Halliday, and Prahalada Krishna Rao. "Thermal modeling in metal additive manufacturing using graph theory–Application to laser powder bed fusion of a large volume impeller." Additive Manufacturing 41 (2021): 101956.
18. Elwarfalli, H., Papazoglou, D., Erdahl, D., Doll, A. & Speltz, J. In Situ Process Monitoring for Laser-Powder Bed Fusion using Convolutional Neural Networks and Infrared Tomography. 2019 Ieee National Aerosp Electron Conf Naecon 00, 323–327 (2019).
19. Ren, Yi Ming, Yichi Zhang, Yangyao Ding, Tao Liu, Cody S. Lough, Ming C. Leu, Edward C. Kinzel, and Panagiotis D. Christofides. "Finite element modeling of direct metal laser solidification process: Sensor data replication and use in defect detection and data reduction via machine learning." Chemical Engineering Research and Design (2021).